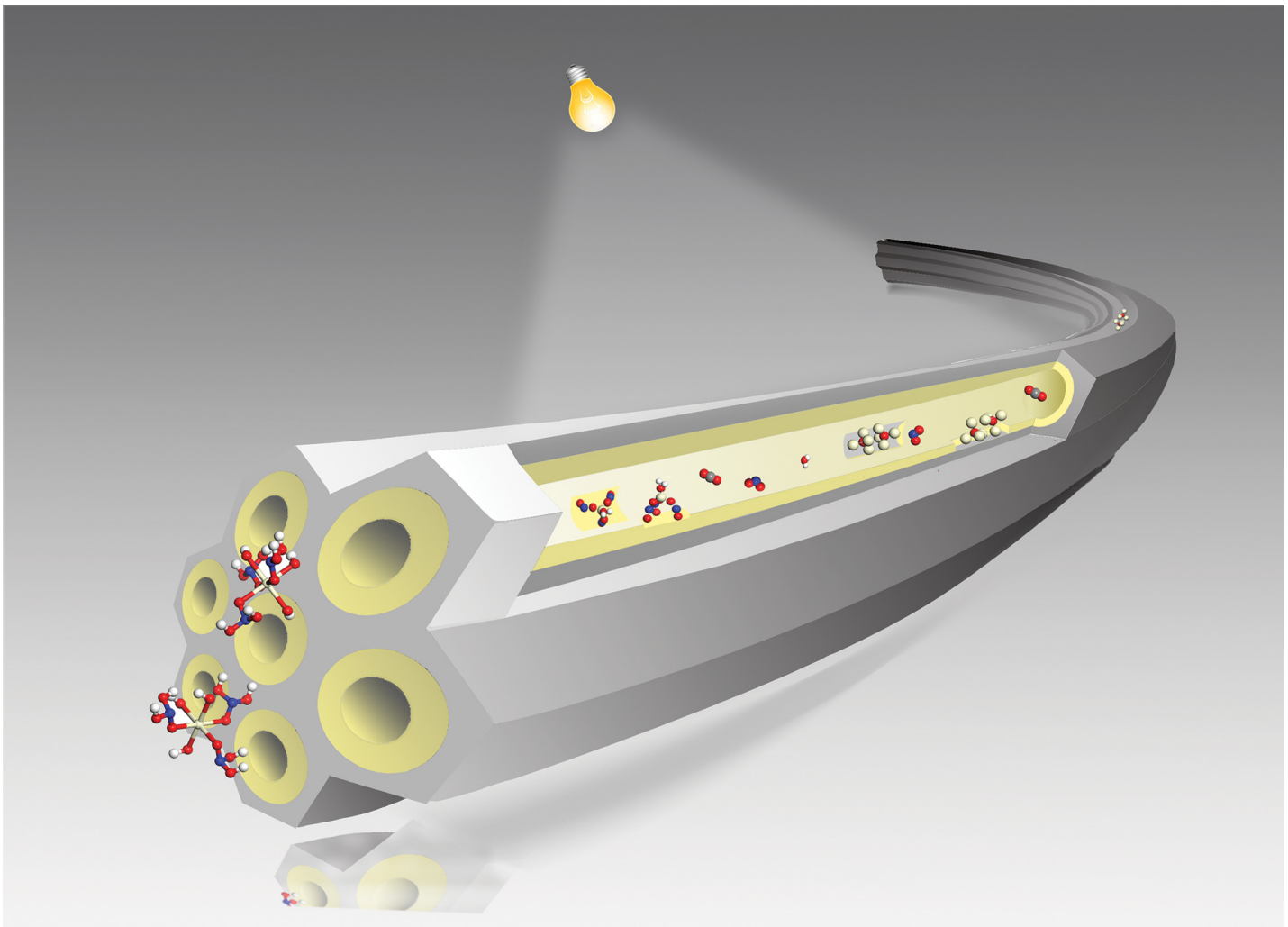

Showcasing research from Professor Hess's laboratory, Department of Chemistry, Technical University of Darmstadt, Germany.

Controlling the dispersion of ceria using nanoconfinement: application to CeO_2/SBA-15 catalysts for NH_3-SCR

Loading the active phase of catalytic materials in a highly dispersed fashion onto porous supports is still a great challenge. As illustrated for ceria-based catalysts, we show that template P123 can be used to control the crystal growth, with direct implications for the catalytic performance. To elucidate the detailed mechanism of this template-assisted synthesis of SBA-15 supported ceria we have applied *in situ* spectroscopies. On this basis, a rational catalyst synthesis was developed by exploiting nanoconfinement effects, resulting in an improved ceria dispersion and superior NH_3-SCR performance.

As featured in:

See Jun Shen and Christian Hess, *Mater. Adv.*, 2021, **2**, 7400.

ROYAL SOCIETY OF CHEMISTRY

rsc.li/materials-advances

Registered charity number: 207890

Materials Advances

ROYAL SOCIETY OF CHEMISTRY

PAPER

View Article Online
View Journal | View Issue

Cite this: *Mater. Adv.*, 2021, 2, 7400

Controlling the dispersion of ceria using nanoconfinement: application to CeO_2/SBA-15 catalysts for NH_3-SCR†

Jun Shen and Christian Hess *

Mesoporous silicas, such as SBA-15, with their high and inert surface area, constitute promising support materials for catalytic applications. However, loading the active phase onto porous materials to give high dispersion and even distribution is still a great challenge. In the presence of the template P123, ceria crystal growth can be controlled by nanoconfinement effects. We have applied *in situ* Raman, DRIFT, and DR UV-vis spectroscopies to elucidate the mechanism of template-assisted synthesis of ceria/SBA-15 catalysts for NH_3-SCR applications. The co-decomposition of P123 and cerium precursor shows a catalytic interaction, resulting in a change of ceria nucleation and growth behavior during the calcination process. Based on this knowledge, we have developed an improved catalyst synthesis by combining the nanoconfinement effects of P123 and the use of an inert atmosphere, resulting in an improved ceria dispersion on SBA-15 and superior NH_3-SCR performance. Our results highlight the significance of the calcination process for defining catalyst properties and the use of *in situ* spectroscopy for rational synthesis of supported catalysts.

Received 28th July 2021,
Accepted 7th September 2021

DOI: 10.1039/d1ma00658d

rsc.li/materials-advances

Introduction

In the past decade, mesoporous materials have attracted great attention due to their high specific surface area, large pore volume, and controllable pore sizes between 2 and 50 nm (according to the IUPAC definition) with extensive applications in gas adsorption, drug delivery, and catalysis.[1] Since the first synthesis of mesoporous SBA-15 by Zhao *et al.*,[2] the enlarged pore sizes (4.6–30 nm) have allowed larger molecules to enter the pore system, and have also decreased the mass transfer limitations compared to conventional zeolites and microporous molecular sieves.[3,4] Due to their inert behaviour in most catalytic reactions, mesoporous silicates are promising support materials for the incorporation of various active compositions, metals or metal oxides, exhibiting a great potential for heterogeneous catalysis.[5–8]

At present, synthetic approaches leading to catalytically active mesoporous silicates are divided into two classes, the "one-pot" strategy and the "loading" strategy.[9] In the case of the "one-pot" strategy (or pre-synthesis method), the silicon source is mixed with the precursor of the active composition, which then both interact with the template to co-assemble into a porous framework.[10–12] This method has the advantage of being a simple operation and the formation of an atomic-scale mixture of active sites in the porous materials, while the additional heteroatom in the framework may destroy the ordered mesoporous structure, leading to further collapses during calcination. The "loading" strategy (or post-synthesis method) mainly involves the preparation of a stable mesoporous silica matrix, followed by its loading with the active composition.[13,14] The bottleneck of this method is the distribution of active species (*e.g.* nanoclusters of metals or metal oxides) inside the long pore channel, which may be susceptible to sintering effects at high-temperature calcination.[15] However, one may envision an intermediate between the pre- and post-synthesis approaches, denoted med-synthesis, in which the template remains in the pore (see Scheme 1) and which,

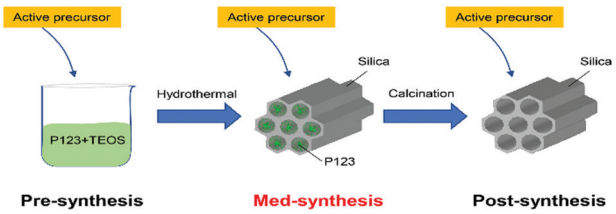

Scheme 1 Synthesis approaches for mesoporous silicate materials (*e.g.* SBA-15) modified by the addition of an active component at different stages.

Eduard-Zintl-Institut für Anorganische und Physikalische Chemie, Technical University of Darmstadt, Alarich-Weiss-Str. 8, 64287 Darmstadt, Germany. E-mail: jun.shen@tu-darmstadt.de, christian.hess@tu-darmstadt.de

† Electronic supplementary information (ESI) available: Additional images and characterization. See DOI: 10.1039/d1ma00658d

although largely ignored for a long time, has the potential to combine the advantages of the pre- and post-synthesis approaches, such as good active phase distribution and defined structure.

Recently, the positive effect of surfactants on the loading of active components in mesoporous silicates has attracted considerable attention. To this end, previous studies have shown that 3 nm-sized ceria particles dispersed on SBA-15, as achieved with the assistance of H_3Cit, caused an enhanced reducibility and defect concentration of the particles, influencing the catalytic performance.[16] Besides, surfactant-assisted impregnation has been widely applied in the context of Ni/SBA-15 catalysts for CO_2 reforming of CH_4.[17] These studies have revealed that the use of surfactant P123 yields a catalytic performance superior to that of other surfactants,[17–20] which was explained by the coordination of Ni atoms by the OH groups of P123, thus preventing their aggregation.[19] Considering that P123 is the template of SBA-15, a method was put forward that used as-made SBA-15 for wetness impregnation after partial removal of P123. This method was employed for the synthesis of Cu/SBA-15 materials, enabling a good dispersion of copper even at high loadings.[21,22] Yin *et al.* suggested an improved method to use the P123-contained SBA-15 combined with solid-state impregnation methods to avoid the extra step of partial removal of P123, which was applied to the synthesis of CuO/SBA-15 for thiophene capture,[23,24] CeO_2/SBA-15 for sulphur capture,[25,26] Pt/SBA-15 for hydrogen storage,[27] Co/SBA-15 for the oxidation of organic pollutants,[28] and Fe/SBA-15 for phenol degradation.[29] Also composite catalysts, *i.e.*, Ag-CeO_2/SBA-15, were prepared by using P123-contained SBA-15, showing good dispersion and catalytic performance for room-temperature reduction of 4-nitrophenol.[30] Summarizing, previous studies have demonstrated the great potential of the template P123-assisted synthesis of mesoporous catalysts containing highly dispersed metals or metal oxides.

Although the med-synthesis approach towards improved supported catalysts has received increasing attention, a detailed mechanistic understanding of the template P123-assisted synthesis is still lacking. One hypothesis is that P123 remaining in the pores of SBA-15 forms a confined space between the silica walls and residual P123 in the intra-wall pores,[22,25–29] while another proposes an interaction between P123 and the metal precursors, influencing their decomposition behavior.[19] However, due to lack of direct experimental evidence, particularly *in situ* analysis, none of the above hypotheses have been verified so far. Besides, it was found that the dispersion effect of P123 was limited to samples with high loadings.[26] Thus, elucidating the mechanism of the template assistance will be of great importance to further improve its applicability to catalyst synthesis.

The selective catalytic reduction (SCR) of NO with NH_3 is an essential process to reduce the emission of NO_x gas, which is known to be harmful to the global environment and human health.[31] Ceria-based materials have been considered as potential catalysts for the NH_3-SCR reaction, due to their high oxygen storage capacity (OSC) and excellent redox properties.[32] Since crystalline CeO_2 cannot provide a sufficiently high specific surface area, especially after high-temperature aggregation, SBA-15 has been employed previously as a support material to disperse and stabilize CeO_2 particles,[33] but also other NH_3-SCR-related materials.[34]

In this contribution, we report how CeO_2/SBA-15 catalysts were prepared by solid-state impregnation methods starting from bare and template-containing SBA-15, aiming at a mechanistic understanding of the synthesis. To monitor the calcination process in detail, *in situ* Raman, DRIFT, and DR UV-vis spectroscopies were applied, revealing details of the transformation of the cerium precursor to the supported oxide. Additional thermogravimetric analysis (TGA) and exhaust gas analysis by FT-IR spectroscopy allowed the temperature-dependent decomposition of the P123 template and the cerium precursors to be monitored. The differently prepared samples were characterized with regard to their structural and surface properties and tested in NH_3-SCR. Based on these combined results, a synthesis mechanism was proposed and used to develop a novel synthesis protocol to yield catalysts with improved ceria dispersion and superior NH_3-SCR performance.

Results and discussion

1. Characterization of dispersed CeO_2 on SBA-15

Three CeO_2/SBA-15 samples were prepared by calcination of the cerium oxide precursor $Ce(NO_3)_3{\cdot}6H_2O$ and the SBA-15 support following different routes, as detailed in Scheme 2. The sample tfSBA–CeO_2–air was synthesized by grinding template-free SBA-15 (tfSBA-15) with cerium nitrate and subsequent calcination in air to obtain ceria crystallites grown inside SBA-15 pores. For the sample asSBA–CeO_2–air, P123-containing SBA-15 (asSBA-15) was employed as support material. Using the same calcination step in air results in ceria dispersed inside the SBA-15 pores. Moreover, a third route was designed, which yields the sample asSBA–CeO_2–N_2, by starting from asSBA-15 but changing the gas atmosphere to inert N_2.

Fig. 1a summarizes the temperature program of the calcination process, which is characterized by two stages, *i.e.*, heating from room temperature to 500 °C at a rate of 1.5 °C min^{-1} and keeping the temperature at 500 °C for 5 h.

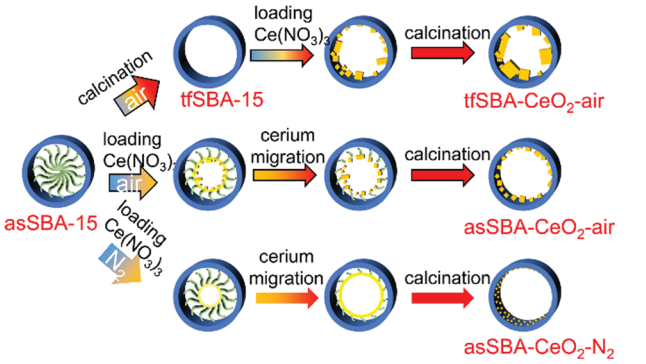

Scheme 2 Different synthesis routes for CeO_2/SBA-15 catalysts using the solid-state impregnation method.

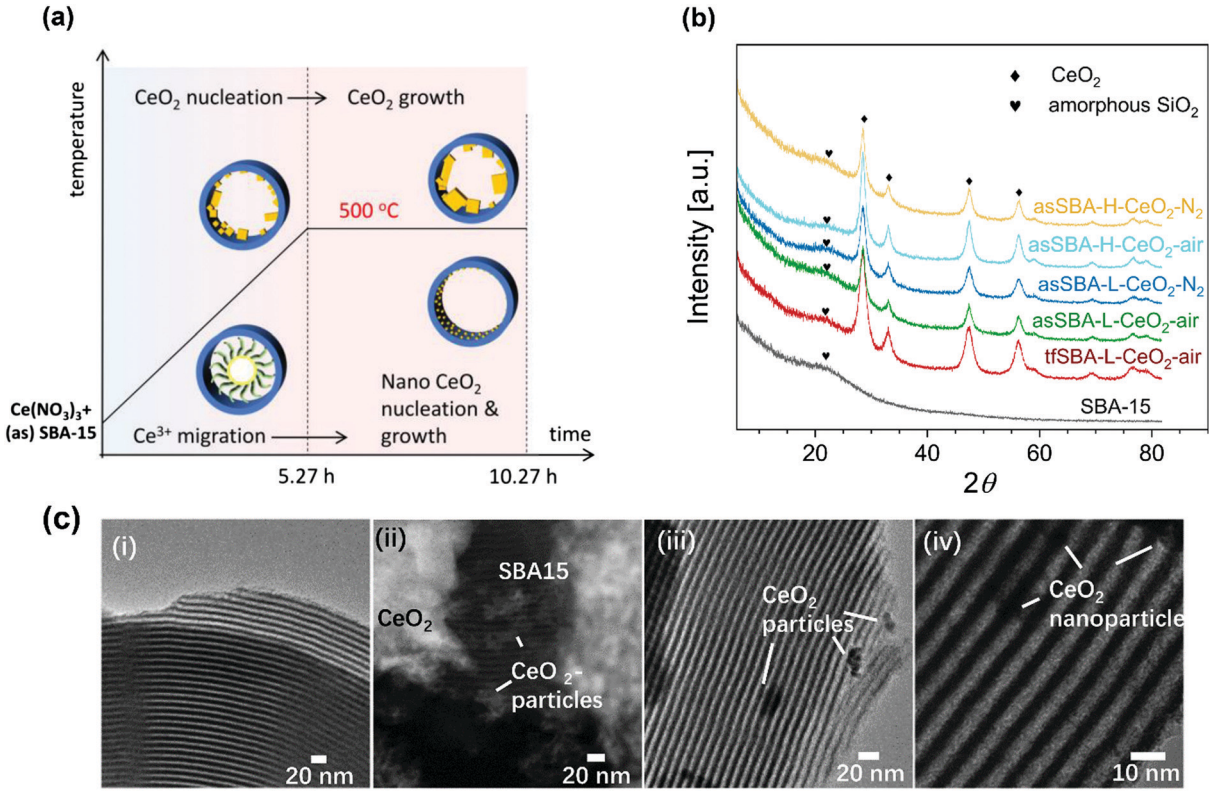

Fig. 1 (a) Temperature program of the calcination process, and (b) XRD patterns of the calcined CeO_2/SBA-15 materials, after start-ing from different SBA-15 matrixes (tfSBA-15 and asSBA-15) and cerium contents (low and high), and applying different atmospheres (air and N_2). For comparison the XRD pattern of bare SBA-15 is shown. The CeO_2-related peaks are marked. XRD patterns are offset for clarity. (c) TEM images of SBA-15 (i), tfSBA–L-CeO_2–air (ii), asSBA–L-CeO_2–air (iii), and asSBA–L-CeO_2–N_2 (iv).

Table 1 Composition, specific surface area, and porosity characteristics of the CeO_2/SBA-15 samples compared to bare SBA-15

Samples	CeO_2 (wt%)	S_{total}[a] [m^2 g^{-1}]	D_p[b] [nm]	V_{micro}[c] [cm^3 g^{-1}]	V_{total}[d] [cm^3 g^{-1}]	d_{CeO_2}[e] [nm]
tfSBA-15	0	616	6.3	0.14	0.64	—
tfSBA–L-CeO_2–air	39	414	6.3	0.06	0.43	7.8
asSBA–L-CeO_2–air	39	359	6.3	0.03	0.39	6.4
asSBA–L-CeO_2–N_2	39	280	5.8	0.02	0.32	5.4

[a] Total BET surface area. [b] Pore diameter determined from the adsorption branch by NLDFT. [c] Micropore volume. [d] Total pore volume. [e] Calculated from XRD results using the Scherrer formula.

Fig. 1b shows wide-angle XRD patterns of the calcined samples. Starting with bare SBA-15, the broad diffraction peak at $2\theta = 23^\circ$ is assigned to amorphous silica. For the samples with CeO_2 loading, new peaks appear at 2θ values of 28.5°, 33.2°, 47.5°, and 56.3°, which can be attributed to different planes of crystalline CeO_2, *i.e.*, (111), (200), (220), and (311), respectively. Detailed analysis reveals that the peaks show a full width at half maximum (FWHM) in the order tfSBA–L-CeO_2–air < asSBA–L-CeO_2–air < asSBA–L-CeO_2–N_2. Based on a fit analysis of the ceria (111) diffraction peak and application of the Scherrer formula,[35] the crystallite sizes are found to decrease as tfSBA–L-CeO_2–air > asSBA–L-CeO_2–air > asSBA–L-CeO_2–N_2 (see Table 1), reflecting the suppression of ceria crystal growth when the use of template P123 is combined with a N_2 calcination atmosphere. Similarly, with increasing CeO_2 loading, the crystallite sizes decreased as asSBA–H-CeO_2–air > asSBA–H-CeO_2–N_2, indicating that an inert calcination atmosphere further improves the CeO_2 dispersion compared to the effect of the surfactant template alone.

Fig. 1c shows TEM bright field images of the calcined samples. The SBA-15 sample (i) has a regular morphology and ordered structure. For the samples tfSBA–L-CeO_2–air (ii), asSBA–L-CeO_2–air (iii), and asSBA–L-CeO_2–N_2 (iv) CeO_2 nanoparticles with decreasing size are observed outside the SBA-15 matrix, showing that similar to XRD TEM detects larger particles but not the highly dispersed ceria inside the pores.

Table 1 summarizes some physical properties of the CeO_2/SBA-15 samples as determined on the basis of N_2 adsorption isotherms, including the specific surface areas, the micropore and total pore volumes, and the pore sizes. The CeO_2-containing

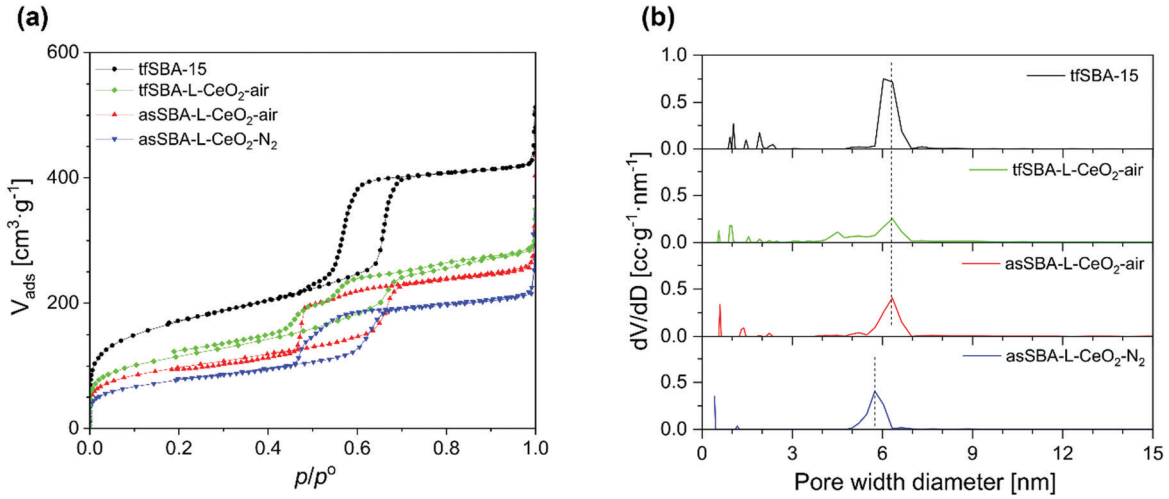

Fig. 2 (a) N_2 adsorption/desorption isotherms, and (b) NLDFT pore size distributions of template-free SBA-15 and CeO_2/SBA-15 materials prepared by different synthesis routes.

samples exhibit smaller specific surface areas than bare template-free SBA-15 (tfSBA-15), decreasing in the order tfSBA–L-CeO_2–air > asSBA–L-CeO_2–air > asSBA–L-CeO_2–N_2, owing to micropore blocking and, in the case of asSBA–L-CeO_2–N_2, also the reduction of mesopore diameter by ceria loading onto the inner surface of the porous matrix.

The N_2 adsorption/desorption isotherms of the SBA-15 and CeO_2/SBA-15 samples all show profiles typical for mesoporous materials (see Fig. 2a), but with variations in the shape of the hysteresis loop. Bare SBA-15 powder shows the typical shape of a mesoporous material with an H1 hysteresis loop at the relative pressure p/p° of 0.55–0.75, reflecting uniform hexagonal pores with a narrow pore size distribution centred around 6.3 nm diameter. For samples loaded with CeO_2, a decrease in the micropore area compared to bare SBA-15 is observed. Also, the closing point of the hysteresis loop shifts to lower relative pressure values of about 0.45, which implies that CeO_2 is formed inside the pores, resulting in open and narrowed mesopores.[36] The desorption branch of the hysteresis loop of tf-SBA-L-CeO_2-air shows two steps, representing open mesopores (p/p° of 0.53–0.70) and narrowed mesopores (p/p° of 0.45–0.53), respectively. For asSBA–L-CeO_2–air, a weak feature from open mesopores and a forced closure of the hysteresis loop at p/p° = 0.46 is observed, which is attributed to ink-bottle type pores. In contrast, the desorption branch of asSBA–L-CeO_2–N_2 is characterized by a smoother decrease, which is somewhat similar to that of SBA-15, representing a more uniform pore size along the channels, while the shift of the curve to lower relative pressure values compared to bare SBA-15 results from the decreased pore size after the coating with CeO_2.

Fig. 2b shows the pore size distributions calculated from the adsorption branches of the isotherms. The samples treated in air, tfSBA–L-CeO_2–air and asSBA–L-CeO_2–air, exhibit a maximum at a pore size of around 6.3 nm, *i.e.*, at the same diameter as the original SBA-15, implying that a considerable amount of surface area inside the pores is uncoated. Especially the pore sizes of tfSBA–L-CeO_2–air are distributed over a wider range towards lower values, suggesting the presence of CeO_2 crystallites inside the pores. In contrast, asSBA–L-CeO_2–N_2 shows a maximum at a decreased pore diameter of 5.8 nm, as a result of a more even coating of the pores with nano-scale CeO_2. For illustration, Fig. S1 in the ESI† provides schematic diagrams of the pore structures of these three samples, as proposed on the basis of the above analysis. In summary, for tfSBA–L-CeO_2–air, the growth of crystalline ceria results in the presence of narrowed pores, while in the case of asSBA–L-CeO_2–air the limited diffusion of the cerium precursor leads to the formation of ink-bottle pores. By contrast, for asSBA–L-CeO_2–N_2, extensive diffusion of cerium ions results in an evenly coated porous matrix.

2. Mechanism of CeO_2 dispersion during calcination

Previously, the good dispersion on asSBA-15 has been proposed to be due to the existence of template P123, resulting in confined spaces for CeO_2 crystal growth, however, without providing direct evidence. To elucidate the interaction between the SBA-15 support and the ceria species during calcination, TG analysis and online gas-phase FTIR spectroscopy, as well as *in situ* Raman, DR UV-vis, and DRIFT spectroscopies were applied.

First, we applied TG analysis to gain detailed insight into the decomposition of the template-containing SBA-15 during calcination, compared to bare asSBA-15 and the cerium precursor $Ce(NO_3)_3{\cdot}6H_2O$ as reference (see Fig. 3a), following the temperature program given in Fig. 1a. The observed thermal decomposition of bare as-made SBA-15 shows a single weight loss of 47 wt% at about 120 °C, which is associated with the decomposition of triblock copolymer P123 slightly embedded in the siliceous pore walls.[37] Previous studies have addressed the decomposition mechanism of bare cerium nitrate $Ce(NO_3)_3{\cdot}6H_2O$ in air by TGA, as summarized in Fig. S2 (ESI†).[38,39] Here, by combining TG and DTG analysis (see Fig. 3a and Fig. S3, ESI†), we

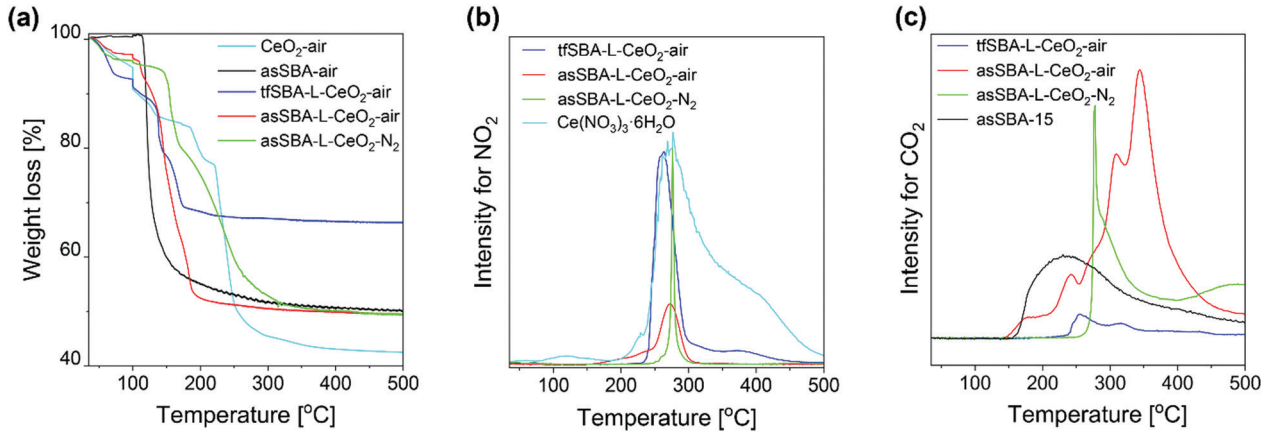

Fig. 3 TGA profiles (a), and IR intensities of exhaust NO_2 (b), and CO_2 (c) during calcination of bare asSBA-15, bare cerium nitrate, and cerium nitrate/SBA-15 mixtures, following the protocol given in Fig. 1a.

identified 221 °C as a critical temperature point, attributed to the onset of cerium nitrate decomposition. Weight losses observed below 221 °C are assigned to the release of surface water and structural water, while at temperatures above 221 °C the decomposition of nitrate resulted in the release of NO_x gas (see below, Fig. 3b) and a further substantial weight loss of 35 wt%. Sample tfSBA–L-CeO_2 calcined in air shows a substantial decrease in weight below 200 °C due to lower onset temperatures for the release of water and cerium nitrate decomposition compared to bare cerium nitrate.

However, because, for the mixed samples (cerium nitrate/SBA-15), the weight loss reflects a more complex interplay of different processes, the exhaust was continuously monitored by gas-phase FTIR spectroscopy. To this end, Fig. 3b depicts the temperature-programmed evolution of NO_2 gas (at 1629 cm^{-1})[40] resulting from cerium nitrate decomposition. As a reference, the NO_2 evolution of bare $Ce(NO_3)_3{\cdot}6H_2O$ salt is shown (see light-blue curve), which is characterized by a sharp increase at 240 °C and a slower decline up to ~500 °C, in agreement with the literature.[39] There is an additional small peak at about 120 °C, indicating the evaporation of aqueous acid azeotrope, as discussed in the context of Fig. S2 (ESI†). Compared to the bare cerium salt, the NO_2 signal of tfSBA–L-CeO_2–air appears within a much narrower temperature range, suggesting the influence of SBA-15 on the decomposition of cerium nitrate. The lack of NO_2 features at lower temperatures, *i.e.*, at around 120 °C and at 190–230 °C, suggests the inhibition of azeotrope formation by dry SBA-15. In contrast, the sample asSBA–L-CeO_2–air shows an increasing signal at 160–250 °C, which is attributed to template P123 decomposition, producing water to form the HNO_3 azeotrope, as well as a stronger nitrate decomposition peak with an onset at ~250 °C. For asSBA–L-CeO_2–N_2, the cerium nitrate precursor is observed to decompose within a very narrow temperature window (250 °C–300 °C), indicating differences in the interaction between precursor and template as a function of the calcination conditions.

Fig. 3c depicts the temperature-programmed evolution of exhaust CO_2 gas (at 2350 cm^{-1})[40] resulting from the decomposition of template P123. For bare as-made SBA-15, the decomposition starts at around 155 °C and extends up to 500 °C. Sample tfSBA15–L-CeO_2–air shows a small feature at 240–350 °C, originating from residual P123 after calcination. By comparison of Fig. 3b and c, it can be seen that the temperature range of the CO_2-related band overlaps with that of the NO_2 band, possibly leading to synergetic effects in the decomposition and oxide formation processes. The sample asSBA–L-CeO_2–air exhibits several CO_2-related peaks. Compared to the single broad CO_2 band detected for bare asSBA-15, these more discrete features indicate the presence of different intermediate states during P123 decomposition. In contrast, when the calcination is performed in N_2, a significant amount of CO_2 is released within a very narrow temperature window (270–275 °C), strongly overlapping with that of the NO_2 release (see Fig. 3b), reflecting an interaction between the decomposition of P123 and that of cerium nitrate, while the CO_2 emission at higher temperatures can be ascribed to the decomposition of oxygen-containing fragments of the template.

To gain more detailed insight into the decomposition processes, Fig. 4 shows the temporal evolution of all exhaust gases during calcination, as detected by online gas-phase IR analysis. Features at around 1150–1250 cm^{-1} are assigned to C–O–C stretching modes,[41] those at 1350 cm^{-1} and 2800–3000 cm^{-1} to C–H bending and stretching modes, respectively.[41] and those at 1750 and 3638 cm^{-1} to C═O and O–H stretching modes, respectively.[40]

For bare asSBA-15, the P123 decomposes directly to gaseous CO_2 as well as C1 or C2 fragments, starting at around 170 °C. In the case of tfSBA–L-CeO_2–air, the decomposition of cerium nitrate, leading to NO_2 formation, and small amounts of CO_2 and C_n ketone are observed from 260 °C onwards. The exhaust gas evolution of asSBA–L-CeO_2–air is characterized by four stages, beginning at about 160 (I), 240 (II), 300 (III), and 350 °C (IV), respectively, consistent with the discrete CO_2 peaks in Fig. 3c: In stage I, C_n fragments (including ketone, alcohol, and ether) are formed, while NO_2 shows a gradual increase, indicating that P123 fragments may affect the decomposition of cerium nitrate, considering the higher onset temperature for

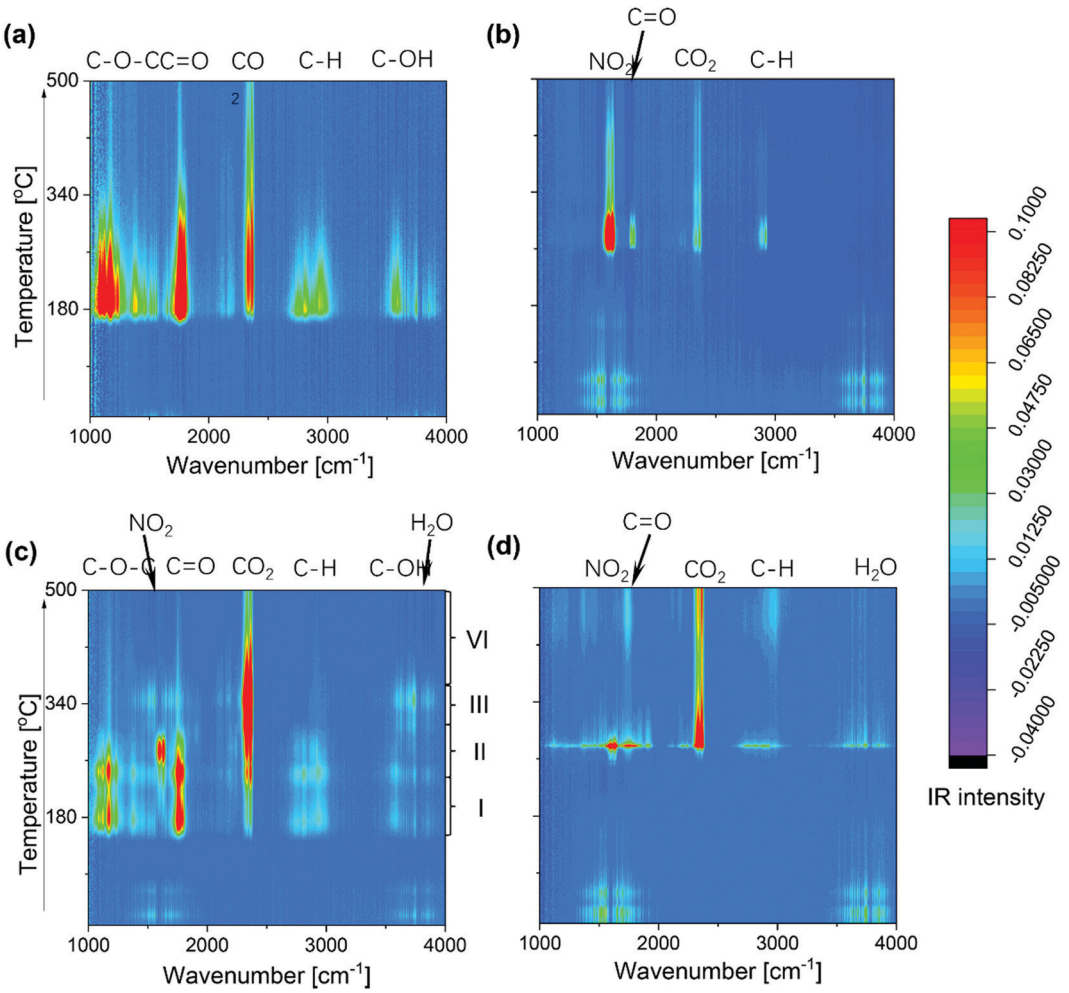

Fig. 4 Online IR detection of exhaust gases during calcination of the samples (a) asSBA15–air, (b) tfSBA–L-CeO_2–air, (c) asSBA–L-CeO_2–air, and (d) asSBA–L-CeO_2–N_2. The low-temperature features at around 1600 and 3750 cm^{-1} can be attributed to water released from cerium nitrate. For details see text.

decomposition observed for tfSBA–L-CeO_2–air. In stage II, which corresponds to the temperature range of the original cerium nitrate decomposition, a facilitated decomposition of P123 compared to bare asSBA-15 is observed, which may be attributed to a catalytic effect by the formed ceria (see below). In stage III, most of the residual P123 is catalytically converted by ceria to CO_2 and H_2O, while in stage IV more stable fragments are decomposed.

Summarizing, from the above *in situ* gas-phase results we conclude that P123 fragments facilitate the decomposition of cerium nitrate, while in turn the formed ceria catalyses the decomposition of P123. Interestingly, for sample asSBA–L-CeO_2–N_2, P123 and cerium nitrate decompose almost simultaneously within a narrow temperature window at about 280 °C, which equals the decomposition temperature of cerium nitrate, according to the tfSBA–L-CeO_2–air and asSBA–L-CeO_2–air results. Thus, we can conclude that the inert atmosphere inhibits the decomposition of P123 at low temperatures (see also Fig. S4, ESI†), allowing an increased catalytic interaction between cerium nitrate and P123 at elevated temperature, boosting the nucleation of nano ceria.

The *in situ* Raman spectra of tfSBA–L-CeO_2–air, asSBA–L-CeO_2–air, and asSBA–L-CeO_2–N_2 during calcination are mainly characterized by Raman features at 457, 745, and 1046 cm^{-1} (see Fig. S5, ESI†). The band at about 460 cm^{-1} is assigned to the triply degenerate symmetrical stretching mode (F_{2g}) of ceria,[42,43] and its position and shape are known to depend on the detailed ceria lattice structure.[44–46] The Raman features at 745 cm^{-1} and 1046 cm^{-1} originate from bending and stretching vibrations of free nitrate, respectively.[47] Fig. 5 compares the temperature-dependent transformation of cerium nitrate into ceria for the three samples, focusing on the nitrate stretching mode at 1046 cm^{-1} to monitor the precursor decomposition (a) and the F_{2g} mode at 457 cm^{-1} to describe formation of crystalline ceria (b). For tfSBA–L-CeO_2–air, the cerium nitrate features disappear at 300 °C, while those for ceria start to appear at 250 °C, implying simultaneous cerium nitrate decomposition and ceria formation. Initially, a broad F_{2g}-related band is detected at about 450 cm^{-1}, which undergoes a narrowing and red-shift to 457 cm^{-1} with increasing temperature, thus indicating the growth of ceria crystallites (see Fig. S5a, ESI†).

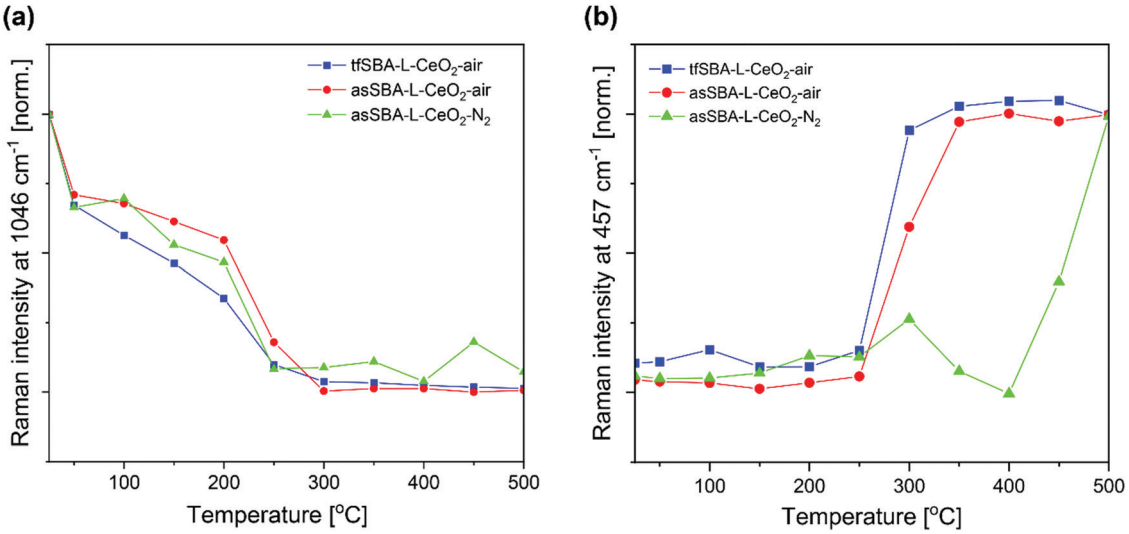

Fig. 5 Temperature-dependent Raman intensities (514.5 nm) at 1046 cm^{-1}, representing cerium nitrate (a), and at 457 cm^{-1}, representing CeO_2 (b), recorded during calcination, following the protocol given in Fig. 1a. The corresponding Raman spectra are shown in Fig. S5 (ESI†).

The additional smaller features at about 250 and 279 cm^{-1} are attributed to nitro- and ceria-related vibrations and discussed in the context of Fig. S5 (ESI†). In the case of the asSBA–L-CeO_2 samples, temperature windows of about 250–300 °C (in air) and 250–450 °C (in N_2) were detected. Sample asSBA–L-CeO_2–air shows the F_{2g} band only at about 300 °C, suggesting an inhibited ceria growth process. In contrast, in the case of asSBA–L-CeO_2–N_2, a F_{2g} band is only indicated, consistent with the presence of amorphous ceria and/or very small ceria crystallites.

Previously, a possible ion-exchange reaction on silicate adsorbent has been reported:[19,48]

$$Ce{-}O{-}NO_2 + OH^- \rightarrow Ce{-}OH + NO_3^- \quad (1)$$

Thus, one may deduce that the dispersion of cerium within the pores is related to the extent of migration of soluble Ce^{3+}, stabilized by hydroxyl groups of P123, prior to forming solid CeO_2 crystallites at higher temperatures. Thus, a wide temperature window is expected to facilitate the migration process of cerium ions within the pores, resulting in a better dispersion.

In situ DR UV-vis spectra were recorded to gain information about changes in the coordination environment of cerium ions during the transformation from $Ce(NO_3)_3$ to CeO_2 (see Fig. 6). The initial DR UV-vis spectra of tfSBA–L-CeO_2–air, asSBA–L-CeO_2–air, and asSBA–L-CeO_2–N_2 at low temperature are characterized by typical features of $Ce(NO_3)_3$ at 218, 255, and 314 nm, which correspond to a $4f^1$-$5d^1$ electronic transfer of Ce^{3+}, a charge transfer (CT) of O^{2-} 2p to Ce^{3+} 4f/5d, and a CT of Ce^{3+} 5d to O^{2-} 2p, respectively.[49] At higher temperature, spectra show a broad absorption band at 220–320 nm, which can be attributed to a CT band of O^{2-} to Ce^{4+} (at ~270 nm) and interband transitions (at ~310 nm) of ceria. With increasing temperature from room temperature to 500 °C, tfSBA–L-CeO_2–air (see Fig. 6a) shows an increase of the bands at 320 nm and 255 nm, but a decrease of the band at 220 nm, which is

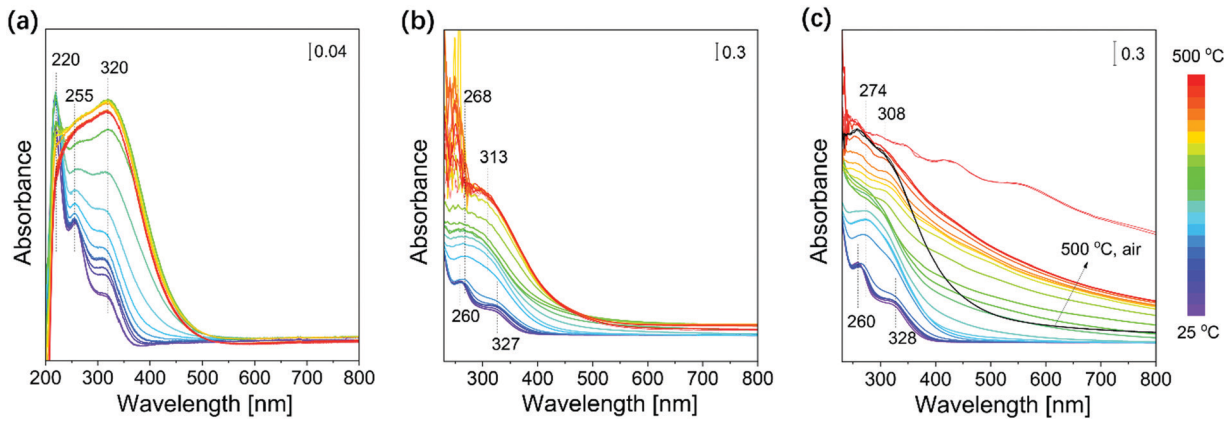

Fig. 6 *In situ* DR UV-vis spectra during the calcination of (a) tfSBA–L-CeO_2–air, (b) asSBA–L-CeO_2–air, and (c) asSBA–L-CeO_2–N_2, following the protocol given in Fig. 1a.

attributed to the transformation of nitrate to oxide. In addition, there is a shift of the absorption edge from 370 nm for $Ce(NO_3)_3$ to 470 nm for CeO_2. For the samples asSBA–L-CeO_2–air (see Fig. 6b) and asSBA–L-CeO_2–N_2 (see Fig. 6c) similar overall changes were observed, *i.e.*, the band at 260 nm increased, while the shoulder band at 320 nm disappeared. The presence of noise signals in the UV region can be explained by the strong absorption of the carbon-containing P123 template. Similarly, the absorption edge shifted from 370 nm to 450 nm for asSBA–L-CeO_2 calcined in air or in N_2/air. The intensity at about 380 and 250 nm has been reported to be proportional to the amount of Ce^{4+} ions in an octahedral/polymeric and a tetrahedral coordination environment of CeO_2, respectively.[50] Thus, we can conclude that there is more tetrahedrally coordinated cerium present in asSBA–L-CeO_2–air/N_2 than in tfSBA–L-CeO_2–air after calcination (see Fig. S6, ESI†).

For bare CeO_2, the direct band gap energy (E_g) can be calculated from the DR UV-vis spectra according to[51]

$$\alpha h\nu = A(h\nu - E_g)^{1/2} \quad (2)$$

where α is the absorption coefficient, which is described by the absorbance here. Using Tauc's method, the evolution of the E_g value during calcination can be derived (see Fig. S7, ESI†). In the low-temperature range, the gradual wavelength blueshift in the UV absorption (*i.e.*, E_g decrease) is due to the removal/dissociation of crystal water and chelated NO_3^- according to[52]

$$Ce(NO_3)_3{\cdot}xH_2O \rightarrow Ce(NO_3)_3(s) \rightarrow CeONO_3\ (s) \rightarrow CeO_{2-x}(s)$$

The E_g values decrease rapidly for tfSBA–L-CeO_2–air to reach a relatively stable state at about 275 °C, while asSBA–L-CeO_2–air and asSBA–L-CeO_2–N_2 require higher temperatures of ~375 °C and 500 °C to reach their final state, respectively. In addition, with increasing temperature from 300 to 500 °C, the band gap energy increases from 2.90 eV to 3.12 eV for tfSBA–L-CeO_2–air, suggesting the growth of CeO_2 crystallites. In contrast, for asSBA–L-CeO_2–air, the band gap reaches its minimum value of 2.85 eV at about 375 °C and then stays unchanged at higher temperature, indicative of a stable ceria crystallite size. Finally, for asSBA–L-CeO_2–N_2, the determined E_g value suggests that there is no dominant ceria crystal phase formation with N_2 at 500 °C, while subsequent calcination for 2 h in air at 500 °C induces an E_g red-shift to 2.71 eV, which may indicate the formation of tiny CeO_2 crystallites.

Fig. 7 shows *in situ* DRIFT spectra of tfSBA–L-CeO_2–air, asSBA–L-CeO_2–air, and asSBA–L-CeO_2–N_2 during the calcination process. The assignments for the observed IR features are summarized in Table S1 (ESI†). Briefly, in the low-wavenumber region (1400–1800 cm^{-1}), mainly bands of nitrogen-containing species, and in the high-wavenumber region (>3000 cm^{-1}) hydroxyl-related features are detected. In addition, there are features attributed to vibrational modes of organic groups, such as C–O, C═O, and C–H, originating from P123 in the case of the asSBA-15-based samples, and from a small amount of residual P123 in the case of the tfSBA-15-based sample. As can be seen in Fig. 7, all three samples exhibit a distinct change in vibrational structure at a critical temperature. In detail, at low temperatures, sample tfSBA–L-CeO_2–air shows a broad band at about 3200–3600 cm^{-1}, originating from H-bonded hydroxyl groups, which disappears when the temperature is raised from 225 °C to 275 °C, suggesting the removal of crystal water from $Ce(NO_3)_3{\cdot}6H_2O$. Simultaneously, a strong decline of the nitrate features (at 1400–1800 cm^{-1}) is detected,[52] indicating the decomposition of cerium nitrate. Similarly, for asSBA–L-CeO_2–air and asSBA–L-CeO_2–N_2, there are rather sudden spectral changes within 225–275 °C and 275–300 °C. These observations further prove that the inert gas causes a delay in the decomposition of the cerium precursor. The asymmetric peak at 3740 cm^{-1} is typical for Si–OH groups, while the feature at 3700 cm^{-1} is attributed to Ce–OH.[45] It is noteworthy that tfSBA–L-CeO_2–air shows a peak at 3740 cm^{-1} over the whole temperature range, providing evidence for the presence of uncovered silica, even after CeO_2 formation. For asSBA–L-CeO_2–air, at the beginning no peak at 3740 cm^{-1} is detected, but at temperatures >275 °C, indicating that surface Si-OH is initially covered by the template, but emerges after the

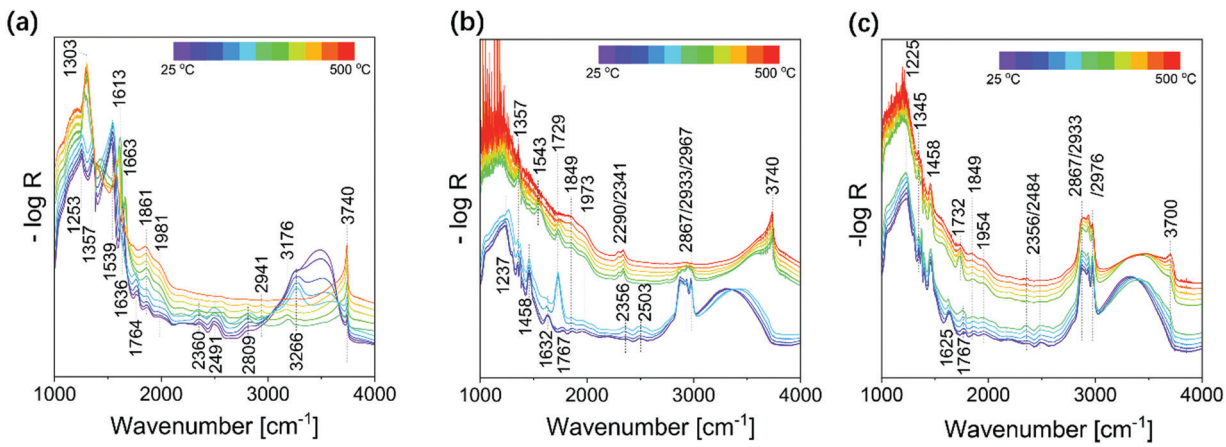

Fig. 7 *In situ* DRIFT spectra during calcination of (a) tfSBA–L-CeO_2–air, (b) asSBA–L-CeO_2–air, and (c) asSBA–L-CeO_2–N_2, following the protocol given in Fig. 1a.

removal of P123. At low temperatures, the sample asSBA–L-CeO_2–N_2 shows spectra similar to those of asSBA–L-CeO_2–air, but the appearance of the Ce–OH peak at 3700 cm^{-1} evidences that the silica surface is coated by ceria. Based on these changes of the surface hydroxyl groups, we can conclude that P123 inside the pores shrinks to the pore wall when the temperature is increased. After reaching a critical temperature, surface Si–OH is exposed. On the other hand, the observation of Ce–OH in the absence of silanol features clearly shows that the formed ceria coats the silica surface.

3. Physical role of P123 in nanoconfinement formation

Previously, it had been proposed that the template could form a confined space to hinder the growth of larger crystallites. An unverified hypothesis was that the confined space was formed between the P123 micelles and the inner wall of SBA-15. As part of our detailed analysis, *in situ* DRIFT spectra show Si–OH-related signals at about 3734 cm^{-1}, which appear after the removal of P123, strongly suggesting that P123 shrinks to the wall with increasing temperature. Especially, at low temperatures, the P123 chains are stabilized by their integration into the silica wall, while in the shrinkage stage, the water loss would break the central micelle structure (see Scheme 3). Thus, P123 tends to shrink to the inner wall, forming a confined space in the pore centre, and cerium ions entering the pore are coordinated by P123, as shown in Scheme 3, overturning previous hypotheses.[29] In the further course of the synthesis, cerium, initially coordinated by P123 in the central confinement,[19] is dispersed onto the silica surface when the template is removed at higher temperatures (see Scheme 3). Besides shrunk P123, carbon (deposited during calcination at higher temperatures) may contribute to the suppression of CeO_2 agglomeration by further confining the space for the ceria growth.

4. Chemical role of P123 for co-catalytic interaction with ceria species

Based on the findings described above, the calcination process involves three steps, *i.e.*, decomposition of cerium nitrate, migration of cerium species, and nucleation/growth of ceria. The final dispersion of ceria is shown to depend on the relative

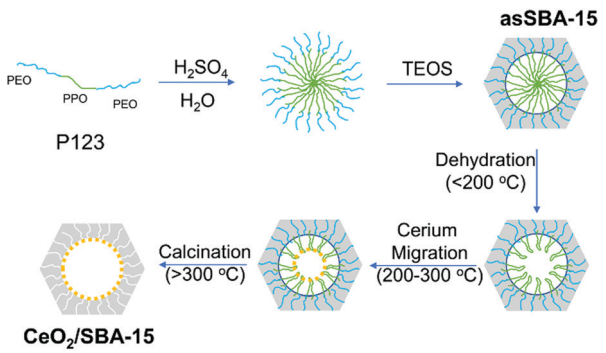

Scheme 3 Schematic diagram of the template-assisted processes leading to ceria dispersion within the mesopores matrix.

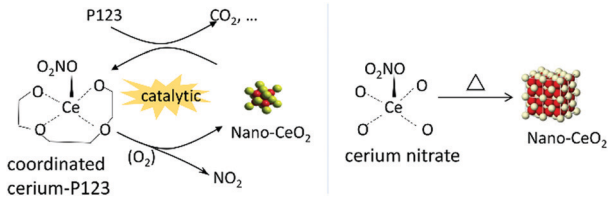

Scheme 4 Calcination of cerium nitrate with (left) or without (right) the assistance of template P123.

decomposition temperatures of P123 and cerium nitrate. The TG and FTIR results have revealed that the decomposition behaviour of cerium nitrate/SBA-15 mixtures significantly deviates from that of bare cerium nitrate and P123 containing SBA-15, confirming the presence of interactions between cerium nitrate and the P123 template.

Calcination of mixed samples in air with the assistance of P123 results in the coordination of cerium ions by P123, while cerium nitrate migrates into the pores.[19] Due to the catalytic reaction between cerium ions and P123, ceria nanoparticles are formed by oxidation in air, while without P123, thermal decomposition of cerium nitrate occurs over a wide temperature range, accompanied by nucleation and growth of ceria crystallites (see Scheme 4). The catalytic reaction facilitates the oxidation of P123-coordinated cerium to ceria nuclei at even lower temperature than the critical decomposition temperature of bare $Ce(NO_3)_3{\cdot}6H_2O$. Meanwhile, reduction by P123 consumes lattice oxygen, which slows down the growth of ceria nanocrystals, thus increasing dispersion of ceria on SBA-15.

Based on the knowledge of the catalytic effect of P123, the synthesis protocol for CeO_2/SBA-15 was modified by application of an inert N_2 atmosphere to further improve the ceria dispersion. Considering the low thermal stability of P123, which decomposes at a temperature of about 115 °C (TGA) in air, the nitrogen atmosphere could delay the decomposition of P123 into carbon chain fragments, thus inhibiting the catalytic oxidation induced formation of ceria nuclei at an early stage until the decomposition temperature of cerium nitrate. Reaching this temperature results in an explosive nucleation of ceria and catalytic decomposition of P123, which is favourable for the formation of a homogeneous nanoscale grain structure.

5. DeNO$_x$ performance

Fig. 8 summarizes the catalytic performance of CeO_2/SBA-15 samples in NH_3-SCR within a temperature range of 100–450 °C. Sample tfSBA–L-CeO_2–air shows the lowest NO conversion (<30%) over the whole temperature range (see Fig. 8a) and the lowest N_2 selectivity in the high-temperature range (see Fig. 8b). The low reactivity in NH_3-SCR is in agreement with that of bare CeO_2 reported previously.[42] Sample asSBA–L-CeO_2–air, which is based on as-made SBA-15 and is calcined in air atmosphere, shows a dramatic improvement in NO conversion and N_2 selectivity, exhibiting a maximum in NO conversion of about 60% at 300 °C. Combining the template interaction with a calcination in inert N_2 atmosphere yields sample asSBA–L-CeO_2–N_2, which shows a further significant increase in NO

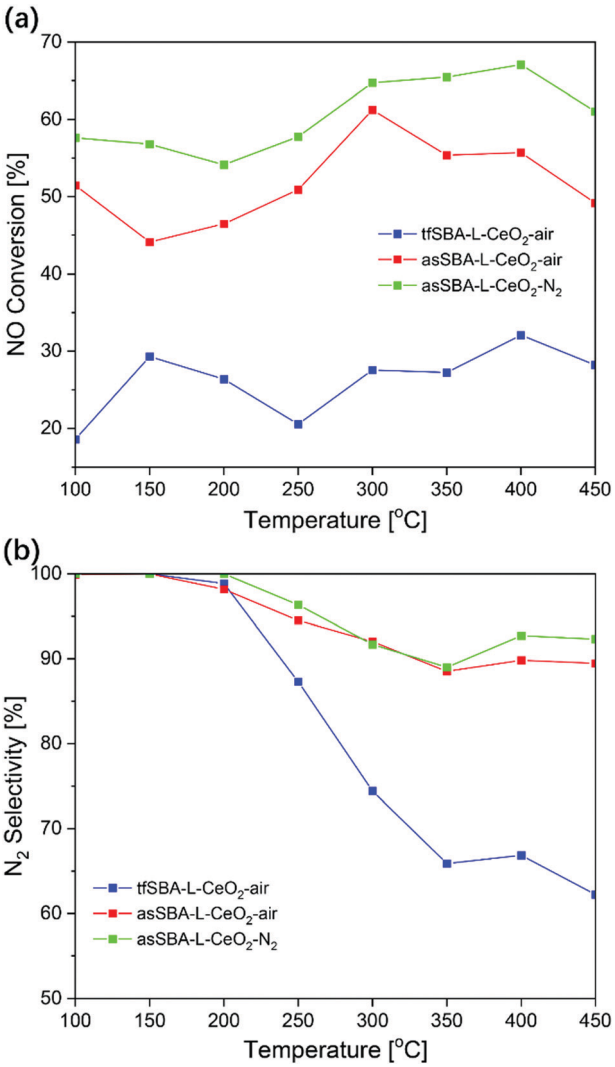

Fig. 8 Catalytic performance of CeO_2/SBA-15 samples in NH_3-SCR. (a) NO conversion and (b) N_2 selectivity. Feed: 500 ppm NO, 500 ppm NH_3, 5% O_2, balanced with N_2; total gas flow: 50 N ml min^{-1}, GHSV = 30 000 h^{-1}. The data points were determined based on an average of five gas-phase IR spectra.

conversion compared to asSBA–L-CeO_2–air, and even the N_2 selectivity slightly improves. Thus, the NH_3-SCR performance of these three samples follows the order asSBA–L-CeO_2–N_2 > asSBA–L-CeO_2–air ≫ tfSBA–L-CeO_2–air, which resembles the extent of ceria dispersion on the SBA-15 surface, as discussed above. In addition, Fig. S9 (ESI†) provides results from a long-term test (20 h) at 300 °C, demonstrating the stability of these samples for NH_3-SCR. At high ceria loading, similar trends were observed (see Fig. S8, ESI†), with overall higher NO conversions compared to low cerium loading. Especially, the N_2 selectivity of asSBA–H-CeO_2–N_2 was significantly higher than that of asSBA–H-CeO_2–air, demonstrating that an inert calcination atmosphere could further improve the CeO_2 dispersion and thus the catalytic performance even at high ceria loading. Table S2 (ESI†) summarizes reactivity data of ceria-based catalysts for NH_3-SCR. In general, pure ceria shows a lower NO_x performance than silica supported ceria, prepared by controlled nanoconfinement thus further improving the ceria dispersion.

Experimental section

1. Materials preparation

asSBA-15 and tfSBA-15. Mesoporous SBA-15 was synthesized according to the methods reported by Zhao *et al.*[2] Briefly, 4 g of pluronic $EO_{20}PO_{70}EO_{20}$ (P123) was dissolved in 150 ml of 1.6 M HCl solution and stirred at 35 °C and a speed of 250 rpm for 2.5 h. Then, 11 ml of tetraethylorthosilicate (TEOS) was added and the obtained mixture was stirred at 35 °C at an increased speed of 400 rpm for 20 h. The stirred mixture was then transferred to a Teflon bottle for hydrothermal treatment and crystallization at 85 °C for 24 h. Vacuum filtration of the suspension at room temperature yielded a white powder, which is referred to as as-made SBA-15 (asSBA-15) and which contains the templating agent P123 in the mesoporous matrix. Calcination of asSBA-15 at 550 °C for 12 h with a heating rate of 1.5 °C min^{-1} in air yields a white powder, referred to as template-free SBA-15 (tfSBA-15), from which the templating agent P123 has been removed.

asSBA–L/H-CeO_2–air/N_2. Cerium nitrate was employed as the cerium source for the preparation of CeO_2/SBA-15 catalysts. The precursor $Ce(NO_3)_3{\cdot}6H_2O$ was mixed with asSBA-15 (see above) *via* solid-state grinding at room temperature for 30 min. The thoroughly mixed powder was then calcined in a muffle furnace at 500 °C for 5 h (heating rate: 1.5 °C min^{-1}) in air (denoted by –air) or N_2 (denoted by –N_2) to remove the P123 template and form the CeO_2 phases. To explore the effect of CeO_2 loading, CeO_2/SBA-15 catalysts with low and high CeO_2 loading were prepared. The sample resulting from a mixture of 0.173 g of $Ce(NO_3)_3{\cdot}6H_2O$ and 0.225 g of asSBA-15 will be referred to as L-CeO_2, while that resulting from a mixture of 0.346 g of $Ce(NO_3)_3{\cdot}6H_2O$ and 0.225 g of asSBA-15 will be labelled as H-CeO_2. Thus, as an example, mixing 0.173 g of $Ce(NO_3)_3{\cdot}6H_2O$ with 0.225 g of asSBA-15, followed by calcination in air, gave the sample asSBA–L-CeO_2–air.

tfSBA–L/H-CeO_2–air/N_2. Similarly, tfSBA-L/H-CeO_2–air/N_2 sam-ples were prepared by following the above protocol, except that asSBA-15 was replaced by tfSBA-15. To ensure comparable CeO_2 loadings, 0.225 g of asSBA-15 was calcined yielding 0.108 g of tfSBA-15. Thus, as an example, mixing 0.173 g of $Ce(NO_3)_3{\cdot}6H_2O$ with 0.108 g of tfSBA-15 followed by calcination in air resulted in the sample tfSBA–L-CeO_2–air.

Prior to catalytic testing in NH_3-SCR, all samples treated in N_2 during synthesis were calcined in air for 2 h at 500 °C to remove residual template.

2. Characterization

XRD. X-ray diffraction experiments were carried out in transmission geometry on an X-ray powder diffractometer (StadiP, Stoe & Cie GmbH) with a Mythen 1K (Dectris) detector. For the measurements, Cu Kα1 radiation (λ = 1.540598 Å) and a Ge[111] monochromator were used.

N_2 adsorption isotherm. Nitrogen adsorption–desorption measurements were carried out on a NOVA 3000e (Quantachrome) to determine the surface area and pore size of the mesoporous samples. The Brunauer–Emmett–Teller (BET) method was employed to calculate the specific surface area, and nonlocal density functional theory (NLDFT) was used to calculate the adsorption branch to obtain the porosity characteristics.

Transmission electron microscopy (TEM). The transmission electron microscope (JEOLJEM-2100F, Tokyo, Japan) is equipped with a Schottky field emitter and was operated at a nominal accelerate voltage of 200 kV. The powder samples were dispersed in ethanol and placed on a carbon grid (Plano).

Thermogravimetric analysis (TGA). TGA was performed on a TGA/SDTA851-e (Mettler Toledo). In order to record TGA curves, samples were exposed to a flow of synthetic air or pure N_2 gas (100 ml min^{-1}) while being heated from room temperature to 500 °C at a rate of 1.5 °C min^{-1}. Samples were then calcined at 500 °C for 5 h. At the same time, derivative thermogravimetry (DTG) profiles were obtained.

Gas-phase Fourier transform infrared (FTIR) spectroscopy. FTIR spectroscopy was performed on a Bruker Tensor 27 equipped with a DLaTGS (deuterated and L-alanine-doped triglycine sulfate) detector, and a low volume gas cell (25 ml, 0.5 m path-length, Axiom). The gas cell was heated to 120 °C to avoid the condensation of water produced by the catalytic reaction. IR spectra were continuously recorded every minute with a resolution of 4 cm^{-1}. The backgrounds used for the analysis were recorded under pure nitrogen gas at room temperature. For online IR gas-phase detection, the Tensor was connected to the SCR reactor (commercial CCR1000 catalyst cell, Linkam Scientific Instruments). The gas-phase concentrations were determined based on a set of calibration curves.

Diffuse reflectance (DR) UV-vis spectroscopy. DR UV-vis spectra were recorded on a Jasco V-770 UV-visible/NIR spectrometer with a praying mantis mirror cell and a high-temperature reaction chamber (Harrick Scientific Products Inc.). Halogen and deuterium light sources were adopted to transmit wavelengths in the visible and ultra-violet, respectively, and a Peltier-cooled PbS detector was employed. Spectra were recorded from 800 to 200 nm with a spectral resolution of 0.5 nm. MgO was used as the white standard.

Raman spectroscopy. Raman spectra were recorded in a backscattering geometry. For excitation, an argon ion laser (514.5 nm, Melles Griot) was employed and for collection of the backscattered light a transmission spectrometer (Kaiser Optical) equipped with a charge-coupled device (CCD) detector was employed. The spectrometer was calibrated using the emission lines of a standard argon lamp. The resolution of the spectrometer was 5 cm^{-1} and the wavelength stability was better than 0.5 cm^{-1}. The laser power was set to 2.5 mW and measured by a power meter (Ophir). The Raman features were fitted by Voigt functions using a Gaussian linewidth of 6 cm^{-1} to account for the instrumental broadening. *In situ* Raman spectra were recorded by using a commercial CCR1000 catalyst cell (Linkam Scientific Instruments).

Diffuse reflectance infrared Fourier transform spectroscopy (DRIFTS). DRIFT spectra were recorded on a Vertex 70 (Bruker) equipped with a liquid N_2 cooled mercury cadmium telluride (MCT) detector and a commercial Harrick cell. As a background standard, KBr powder was used. The spectral resolution of DRIFTS was 1 cm^{-1}, the temporal resolution was 60 s. *In situ* DRIFT spectroscopy was combined with gas-phase analysis, by analyzing the gas phase at the outlet of the *in situ* cell by gas-phase FTIR spectroscopy (see above).

3. Catalytic tests

The SCR performance of the catalysts was measured in a commercial CCR1000 reactor (Linkam Scientific Instruments) in combination with quantitative gas-phase FTIR spectroscopy (see above). The flow rate of the inlet gases was adjusted by mass flow controller, by employing the following gas sources: 2000 ppm NO/N_2 (±0.25% abs.), 2000 ppm NH_3/N_2 (±0.25% abs.), O_2 (≥99.999%), and N_2 (≥99.999%). For catalytic testing in NH_3-SCR, the concentrations of NO, NH_3, and O_2 in the feed gas mixture were set to 500 ppm, 500 ppm, and 5%, respectively, and balanced with N_2. The weight of the catalyst samples loaded into the reactor was 15 mg; the feed gas mixture passed through the catalyst bed at a total flow rate of 50 ml min^{-1}, resulting in a gas hourly space velocity (GHSV) of 30 000 h^{-1}.

Using the detected concentrations of NO, NO_2, N_2O, and NH_3 in the outlet gas flow, and the feed gas concentrations, the N_2 concentration can be calculated based on conservation of mass, assuming that besides N_2 nitrogen is present only in the form of the gases listed above. NO_x conversion and N_2 selectivity were calculated using the following equations:

$$\text{NO conversion} = \frac{[\text{NO}]_{\text{in}} - [\text{NO}]_{\text{out}}}{[\text{NO}]_{\text{in}}} \times 100\% \quad (3)$$

$$\text{N}_2\text{ selectivity} = \frac{[\text{N}_2]_{\text{out}}}{[\text{N}_2]_{\text{out}} + [\text{N}_2\text{O}]_{\text{out}}} \times 100\% \quad (4)$$

where the subscripts in and out indicate the inlet and outlet flows of the reactor, respectively.

Conclusions

Herein, we have reported our studies of the synthesis mechanism of CeO_2/SBA-15 catalysts by the solid-state impregnation method using a combination of TG and IR gas-phase analysis, as well as *in situ* Raman, DR UV-vis, and DRIFT spectroscopies. These studies have revealed that ceria formation on mesoporous SBA-15 during calcination involves first cerium precursor decomposition, then migration of cerium species, and finally ceria formation at high temperature. Based on our findings we can explain the roles of the template inside the mesoporous matrix: on one hand P123 acts as a physical barrier to prevent the growth of ceria, on the other, P123 acts as a chemical reactant, which interacts with cerium ions, thus enabling the catalytic decomposition of the cerium precursor.

With the gained mechanistic knowledge of the formation of CeO_2/SBA-15 materials, a new calcination protocol was

developed based on an intended retardation of the decomposition of the template and the cerium precursor, leading to a higher dispersion of ceria inside the pores and thus a significant improvement of catalytic performance in NH_3-SCR.

An important finding of the study is that the precursor itself can facilitate the synthesis of the catalyst, as demonstrated here for a ceria-based catalyst, by using both the template and the gas atmosphere to control the catalytic reaction conditions. Our results underline the importance of the details of the calcination process for defining the catalyst properties. Application of *in situ* spectroscopy allows one to monitor the preparation process, including calcination, thus facilitating a rational synthesis of supported catalysts as shown here in the context of NO_x abatement. The outlined approach is expected to trigger more studies on the development of improved catalysts based on a careful design of the catalytic preparation reactions.

Author contributions

The manuscript was written through contributions of both authors. Original idea, C. H.; conceptualization, J. S. and C. H.; methodology, J. S.; formal analysis, J. S.; writing – original draft preparation, J. S.; writing – review and editing, C. H.; supervision, C. H.; project administration, C. H.

Conflicts of interest

There are no conflicts to declare.

Acknowledgements

The authors thank Martin Brodrecht for N_2 adsorption–desorption measurements, Kathrin Hofmann for XRD analysis, Stefan Lauterbach for TEM analysis, and Karl Kopp for XPS analysis and technical support. Financial support by the Deutsche Forschungsgemeinschaft (DFG) is gratefully acknowledged.

Notes and references

1 W. Li, J. Liu and D. Y. Zhao, *Nat. Rev. Mater.*, 2016, **1**, 1–17.
2 D. Y. Zhao, J. L. Feng, Q. S. Huo, N. Melosh, G. H. Fredrickson, B. F. Chmelka and G. D. Stucky, *Science*, 1998, **279**, 548–552.
3 F. Khanmohammadi, M. A. Molina, R. M. Blanco, S. N. Azizi, C. Marquez-Alvarez and I. Diaz, *Microporous Mesoporous Mater.*, 2020, **309**, 1–6.
4 S. Inagaki, S. Guan, Y. Fukushima, T. Ohsuna and O. Terasaki, *J. Am. Chem. Soc.*, 1999, **121**, 9611–9614.
5 J. Nakazawa, B. J. Smith and T. D. P. Stack, *J. Am. Chem. Soc.*, 2012, **134**, 2750–2759.
6 S. F. Zhang, B. Zhang, H. J. Liang, Y. Q. Liu, Y. Qiao and Y. Qin, *Angew. Chem., Int. Ed.*, 2018, **57**, 1091–1095.
7 P. Hongmanorom, J. Ashok, G. H. Zhang, Z. F. Bian, M. H. Wai, Y. Q. Zeng, S. B. Xi, A. Borgna and S. Kawi, *Appl. Catal., B*, 2021, **282**, 119564.
8 C. Hess, in *Comprehensive Inorganic Chemistry II*, ed. J. Reedijk and K. Poeppelmeier, Elsevier, Amsterdam, 2013, vol. 7.
9 V. Chaudhary and S. Sharma, *J. Porous Mater.*, 2017, **24**, 741–749.
10 P. Hongmanorom, J. Ashok, S. Das, N. Dewangan, Z. Bian, G. Mitchell, S. Xi, A. Borgna and S. Kawi, *J. Catal.*, 2020, **387**, 47–61.
11 R. R. Chada, S. S. Enumula, K. S. Reddy, M. D. Gudimella, S. R. R. Kamaraju and D. R. Burri, *Microporous Mesoporous Mater.*, 2020, **300**, 110144.
12 O. Daoura, G. Fornasieri, M. Boutros, N. El Hassan, P. Beaunier, C. Thomas, M. Selmane, A. Miche, C. Sassoye, O. Ersen, W. Baaziz, P. Massiani, A. Bleuzen and F. Launay, *Appl. Catal., B*, 2021, **280**, 119417.
13 J. W. Fan, X. F. Niu, W. Teng, P. Zhang, W. X. Zhang and D. Y. Zhao, *J. Mater. Chem. A*, 2020, **8**, 17174–17184.
14 R. A. Mitran, D. C. Culita and I. Atkinson, *Microporous Mesoporous Mater.*, 2020, **306**, 110484.
15 R. Manno, P. Ranjan, V. Sebastian, R. Mallada, S. Irusta, U. K. Sharma, E. V. Van der Eycken and J. Santamaria, *Chem. Mater.*, 2020, **32**, 2874–2883.
16 N. N. Mikheeva, V. I. Zaikovskii and G. V. Mamontov, *Microporous Mesoporous Mater.*, 2019, **277**, 10–16.
17 C. Chong, A. H. K. Owgi, N. Ainirazali, S. Y. Chin and H. D. Setiabudi, *Mater. Today: Proc.*, 2018, **5**, 21644–21651.
18 S. N. Bukhari, A. H. K. Owgi, N. Ainirazali, D. V. N. Vo and H. D. Setiabudi, *Mater. Today: Proc.*, 2018, **5**, 21620–21628.
19 W. W. Yang, H. M. Liu, Y. M. Li and D. H. He, *Microporous Mesoporous Mater.*, 2016, **228**, 174–181.
20 W. W. Yang, H. M. Liu, Y. M. Li, H. Wu and D. H. He, *Int. J. Hydrogen Energy*, 2016, **41**, 1513–1523.
21 B. Dragoi, G. Laurent, S. Casale, T. Benamor, B. Lebeau, C. Boissiere, F. Ribot, M. Selmane, P. Schmidt, D. Kreher and A. Davidson, *J. Sol–Gel Sci. Technol.*, 2019, **91**, 552–566.
22 B. Dragoi, I. Mazilu, A. Chirieac, C. Ciotonea, A. Ungureanu, E. Marceau, E. Dumitriu and S. Royer, *Catal. Sci. Technol.*, 2017, **7**, 5376–5385.
23 Y. Yin, W. J. Jiang, X. Q. Liu, Y. H. Li and L. B. Sun, *J. Mater. Chem.*, 2012, **22**, 18514–18521.
24 Y. Yin, P. Tan, X. Q. Liu, J. Zhu and L. B. Sun, *J. Mater. Chem. A*, 2014, **2**, 3399–3406.
25 Y. Yin, D. M. Xue, X. Q. Liu, G. Xu, P. Ye, M. Y. Wu and L. B. Sun, *Chem. Commun.*, 2012, **48**, 9495–9497.
26 Y. Yin, Z. H. Wen, X. Q. Liu, A. H. Yuan and L. Shi, *Adsorpt. Sci. Technol.*, 2018, **36**, 953–966.
27 Y. Yin, Z. F. Yang, Z. H. Wen, A. H. Yuan, X. Q. Liu, Z. Z. Zhang and H. Zhou, *Sci. Rep.*, 2017, **7**, 4509.
28 Y. Yin, H. Wu, L. Shi, J. Q. Zhang, X. Y. Xu, H. Y. Zhang, S. B. Wang, M. Sillanpaad and H. Q. Sun, *Environ. Sci.: Nano*, 2018, **5**, 2842–2852.
29 Y. Yin, L. Shi, W. L. Li, X. N. Li, H. Wu, Z. M. Ao, W. J. Tian, S. M. Liu, S. B. Wang and H. Q. Sun, *Environ. Sci. Technol.*, 2019, **53**, 11391–11400.
30 A. Taratayko, Y. Larichev, V. Zaikovskii, N. Mikheeva and G. Mamontov, *Catal. Today*, 2021, **375**, 576–584.

31 L. P. Han, S. X. Cai, M. Gao, J. Hasegawa, P. L. Wang, J. P. Zhang, L. Y. Shi and D. S. Zhang, *Chem. Rev.*, 2019, **119**, 10916–10976.
32 A. Trovarelli, *Catal. Rev.*, 1996, **38**, 439–520.
33 J. Strunk, W. C. Vining and A. T. Bell, *J. Phys. Chem. C*, 2011, **115**, 4114–4126.
34 J. Shen and C. Hess, *Catalysts*, 2020, **10**, 1386.
35 M. T. Weller, *Inorganic materials chemistry*, Oxford University Press, Oxford; New York, 1994.
36 J. P. Thielemann, F. Girgsdies, R. Schlogl and C. Hess, *Beilstein J. Nanotechnol.*, 2011, **2**, 110–118.
37 S. Y. Chen, T. Mochizuki, Y. Abe, M. Toba, Y. Yoshimura, P. Somwongsa and S. Lao-ubol, *Appl. Catal., B*, 2016, **181**, 800–809.
38 E. A. Cochran, K. N. Woods, D. W. Johnson, C. J. Page and S. W. Boettcher, *J. Mater. Chem. A*, 2019, **7**, 24124–24149.
39 W. Kang, D. O. Ozgur and A. Varma, *ACS Appl. Nano Mater.*, 2018, **1**, 675–685.
40 N. Ulagappan and H. Frei, *J. Phys. Chem. A*, 2000, **104**, 7834–7839.
41 Y. L. Liu and H. J. Kim, *Sensors*, 2017, **17**, 1469.
42 B. L. Zhang, S. G. Zhang and B. Liu, *Appl. Surf. Sci.*, 2020, **529**, 147068.
43 W. H. Weber, K. C. Hass and J. R. Mcbride, *Phys. Rev. B: Condens. Matter Mater. Phys.*, 1993, **48**, 178–185.
44 T. Suzuki, I. Kosacki, H. U. Anderson and P. Colomban, *J. Am. Ceram. Soc.*, 2001, **84**, 2007–2014.
45 A. Filtschew, K. Hofmann and C. Hess, *J. Phys. Chem. C*, 2016, **120**, 6694–6703.
46 C. Schilling, A. Hofmann, C. Hess and M. V. Ganduglia-Pirovano, *J. Phys. Chem. C*, 2017, **121**, 20834–20849.
47 A. Filtschew, D. Stranz and C. Hess, *Phys. Chem. Chem. Phys.*, 2013, **15**, 9066–9069.
48 J. Seo, J. W. Lee, J. Moon, W. Sigmund and U. Paik, *ACS Appl. Mater. Interfaces*, 2014, **6**, 7388–7394.
49 V. Nicolini, E. Varini, G. Malavasi, L. Menabue, M. C. Menziani, G. Lusvardi, A. Pedone, F. Benedetti and P. Luches, *Mater. Des.*, 2016, **97**, 73–85.
50 C. M. Aiube, K. V. de Oliveira and J. L. de Macedo, *Catalysts*, 2019, **9**, 377.
51 S. Phokha, S. Pinitsoontorn, P. Chirawatkul, Y. Poo-arporn and S. Maensiri, *Nanoscale Res. Lett.*, 2012, **7**, 425.
52 C. X. Wang, D. Z. Ren, J. C. Du, Q. G. Qin, A. M. Zhang, L. Chen, H. Cui, J. L. Chen and Y. K. Zhao, *Catalysts*, 2020, **10**, 143.